Optimization of Pinned Photodiode Pixels for High-Speed Time of Flight Applications

**FABIO ACERBI [1] (Member, IEEE), MANUEL MORENO-GARCIA[1] (Member, IEEE), GÖZEN KÖKLÜ[2],
RADOSLAW MARCIN GANCARZ[2], BERNHARD BÜTTGEN[2], (Member, IEEE), ALICE BIBER[2],
DANIEL FURRER[2], AND DAVID STOPPA[2] (Member, IEEE)**

1 Center for Material and Microsystems, Fondazione Bruno Kessler, I-38123 Trento, Italy
2 Heptagon Advanced Micro Optics Pte Ltd, AMS AG, Advanced Optical Sensors Division, CH-8803 Rüschlikon, Switzerland

CORRESPONDING AUTHOR: F. ACERBI (e-mail: acerbi@fbk.eu)

ABSTRACT We discuss optimizations of pinned photodiode (PPD) pixels for indirect time of flight sensors. We focus on the transfer-gate and dumping gate regions optimization, on the PPD dimension and shape to assure fast lateral charge transfer and on the epitaxial layer thickness for a good tradeoff between fast vertical charge transfer and high quantum efficiency at near infrared region. The overall performance of the pixel is quantified by the demodulation contrast of the pixel at specific frequencies. The operation frequency of the device is determined by the required ambiguity range of the application and the required distance noise. In order to reach a reasonable distance noise, the pixel needs to allow modulation frequencies up to 100 MHz. In this paper, we present TCAD simulation and experimental data on demodulation contrast, impulse response time, and quantum efficiency of $10 \times 10 \ \mu$m pixels. We introduce a setup for impulse response measurement and we compare this to the demodulation contrast. We also discuss the optimization of the dump gate and dump diffusion. With the best pixel we measured a quantum efficiency of about 45% at 850 nm, a demodulation contrast of 47% at 80 MHz, and an impulse response time < 5 ns.

INDEX TERMS Pinned photodiode, time-of-flight, ToF, transfer gate, dump gate, distance measure.

I. INTRODUCTION

In recent years, there has been a massive development in 3D vision systems (i.e., range imagers), driven mainly by market requirements in gaming, automotive and mobile applications. In such systems, the Time-of-Flight (ToF) technique is emerging over the others [1], [2]. ToF relies on the measurement of time delay (direct ToF) or phase shift (indirect ToF) between the light pulses emitted by the active illuminator and the received light backscattered from the objects in the scene. The indirect ToF working principle is represented in Fig. 1 where there is a sinusoidal-modulated illumination and an iToF camera to detect the reflected light [3].

Some photodetector technologies have been proposed in the literature for indirect ToF applications ("demodulation pixels" [4], "lock-in pixels" [5] based on CCD/CMOS technology, and current assisted photo-demodulators [6], [7]). Optimized Pinned photodiodes (PPD) feature several key advantages over other photo-detector technologies.

In general, they are realized in CMOS Image Sensor (CIS) processes and they do not necessarily require a major process customization other than pixel implant customization for fast charge transfer [8], [9]. They can have very compact pixel pitch enabling high-resolution imagers, low dark current, thanks to the surface shielding, and possibly less number of masks for CIS process customization compared to others.

Generally, a photodetector (PD) structure for iToF is composed by a photosensitive area and a collection node (tap), where the charge is accumulated during the integration cycles, synchronously with the modulation of the light [1], [2]. In the literature, there are examples of ToF pixels with one, two or more number of collection nodes for demodulation and for anti-blooming [11]. Others instead, use an approach with three or more collection nodes [12]. For example, for a detector with two taps and when the scene is illuminated with a modulated NIR light source, the charge is collected at first in the two taps with clock
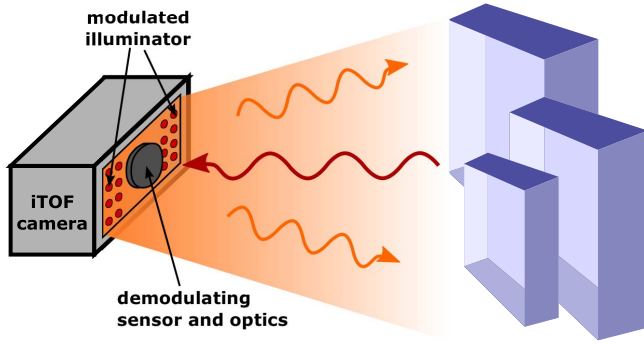
See http://www.ieee.org/publications_standards/publications/rights/index.html for more information.

FIGURE 1. Basic principle of indirect Time-of-flight camera measurements: pulsed light is shined over the target and the camera demodulates the reflected light and creates the 3D image.

FIGURE 2. Schematized cross-section example of a generic pinned photodiode (PPD) structure along the transfer-gate (TG) region. The different implants and the STI regions are highlighted: the n+ implant creating the floating diffusion (FD), the threshold adjustment implant, the p+ pinning layer (PPDp) and the customized storage n-well of the PPD (PPDn). Distance "d1" is between p-well mask and TG edge.

signal synchronous with the light modulation (one tap is in-phase and the second one is with opposite phase), creating the 0° and 180° signals, and then with the clock signal delayed properly, it accumulates the 90° and 270° signals [1], [5], [10].

After collecting charges at different phases in different taps (0°, 90°, 180°, 270°, getting the signals A_0, A_1, A_2, A_3), we can calculate the offset (B), amplitude (A) and demodulation contrast of a pixel with the following formulas [4], [5]:

$$B = \frac{A_0 + A_1 + A_2 + A_3}{4} \qquad (1)$$

$$A = \frac{\sqrt{(A_0 - A_2)^2 + (A_1 - A_3)^2}}{2} \qquad (2)$$

$$C_{demod} = \frac{A}{B} = \frac{meas\_amplitude}{meas\_offset} \qquad (3)$$

Considering the state-of-the-art iToF sensors, there are typically two main targets to reach: i) demodulation frequency in the order of 100 MHz with >40% demodulation contrast and ii) as high as possible Quantum Efficiency (QE) in the near infrared (NIR) region, i.e., between 850 nm and 950 nm, which are the typical wavelengths used in ToF systems in order to reduce the required optical power to compensate for the sunlight impact on the system performance and to avoid a visible light during operation in order to maximize user experience [5]. In addition, the iTOF pixels require a relatively large full-well capacity (FWC) of the floating diffusion region, i.e., the maximum charge that can be stored (confined) in this region without "spilling-out". This is because during the accumulation time period the collected charge is always directed towards one of the floating diffusions and it is important that this does not "spill" over into another one. In iToF application the full-well capacity is also "consumed" by sunlight power.

In this work, we discuss about the optimization of the PPD structure to reach the best performance for iToF applications. In particular, we analyze and optimize the implants and the layout of the PPD to reach both a high transfer speed and high quantum efficiency. In particular, the charge transfer, is composed by two elements: i) the vertical transfer of
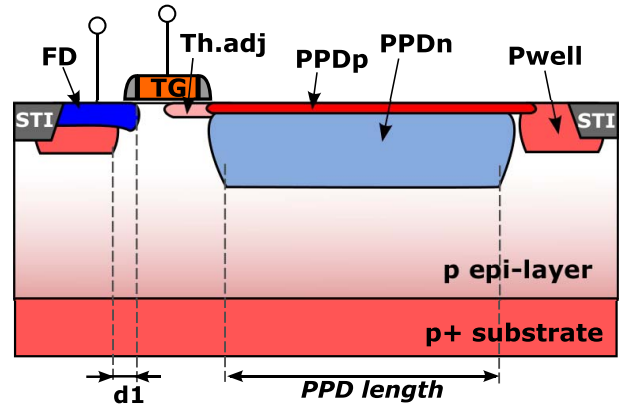
the photo-generated charges in the silicon epi-layer, which are drifted towards the PPD high-potential region (i.e., the conduction band well), and ii) the lateral charge transfer from the PPD region to one of the collection nodes (i.e., the floating diffusions) through the relative transfer gate (TG). When using thick epi-layer, for example to improve the QE, the vertical transfer component becomes important.

II. PPD OPTIMIZATION BASED ON TCAD SIMULATIONS

The simplified cross-section of a pinned photodiode is shown in Fig. 2, highlighting, in particular, the PPD region, made by the PPD p-type and PPD n-type implants, the transfer gate (TG) region with the threshold adjustment implant and the floating diffusion region.

In this work we focus on several important optimization points: i) p-well to TG edge distance, which is d1 in Fig. 2, ii) the threshold adjustment implant, iii) the PPD dimensions and shape, iv) dump gate region optimization v) epitaxial layer thickness optimization and trade-offs.

The dump gate will be better detailed in the next chapters. Its function in iToF pixels, is to guarantee a spilling path for charge during pixel readout when all TG are open (not conductive).

We employed a customized 3D full TCAD simulation deck (based on Synopsys Sentaurus simulation software), optimized for the specific manufacturing process. We prepared several types of simulations to validate the pixel performance, which will be described in this section.

A. CONDUCTION BAND ENERGY (CBE)

In this simulation the bias voltages of FD and TG were ramped towards the proper values and we plotted the equipotential lines or the conduction band energy inside the PPD and FD. See for example Fig. 4. With these simulations, we analyze if there are undeplated regions, barriers or pockets in the pixel and we do necessary modifications to remove these artifacts.

B. IMPULSE RESPONSE TIME

The biases in the FD and the TG were ramped towards the proper values, then we performed a transient simulation where the light excitation is composed by a pulse, lasting 500ns, with <1ns rise and fall times. We analyzed the FD current vs. time in response to light pulse and we obtained the impulse response time as the required time for the signal to reach from 10% to 90% of the final value. As can be seen in Fig. 6, with these simulations, we can identify the fastest pixel and can also understand the root cause of the slowness or fastness of a pixel in relation to CBE graphs.

C. STATIC CONTRAST

With the PPD properly biased as in previous points, we compared the value of the FD current with TG ON and TG OFF conditions. From this simulation, the static contrast of the pixel (i.e., the contrast obtained in a static regime, not modulating the light) can be calculated as:

$$C_{static} = \frac{I_{ON} - I_{OFF}}{I_{ON} + I_{OFF}} \qquad (4)$$

This simulation allows to identify possible cross-talk or leakage from one tap to another, which would make us lose the modulation information.

III. PIXEL OPTIMIZATION

By means of the previous simulation types we optimized the PPD performance, in particular we focused on: i) lateral and vertical charge transfer, ii) depletion depth, iii) pinning voltage, iv) quantum efficiency, and v) sunlight performance.

To do that, we tailored the PPD structure, in particular some specific and important points: i) the p-well mask edge position, ii) an additional transfer-gate threshold adjustment implant, iii) the PPD length and shape, iv) the addition of a dumping gate and v) epitaxial layer thickness. These points are discussed in the following sections.

A. P-WELL MASK POSITION

The PPD region is typically without any p-well or n-well beneath it, since it is important to have a high depletion depth to increase the QE at long wavelengths. The p-well stops beneath the FD, and its mask-edge position can be tailored to have the right TG modulation on the channel that is created between FD and PPD. This is generally not deeply discussed in other works, which instead may use other custom implants to avoid punch-through [13].

We report here the TCAD simulations with four different p-well-to-TG distances, where the difference between the largest and smallest value of this distance is 1 μm. We do not report here the absolute numbers since they depend on the actual technology and implants used.

Fig. 3 shows the doping concentration and Fig. 4 represents the relative conduction band energy. With p-well extending under the TG, in other words with the smaller distance between p-well to TG (dist1), the channel between the PPD and the FD is too small, creating a high potential
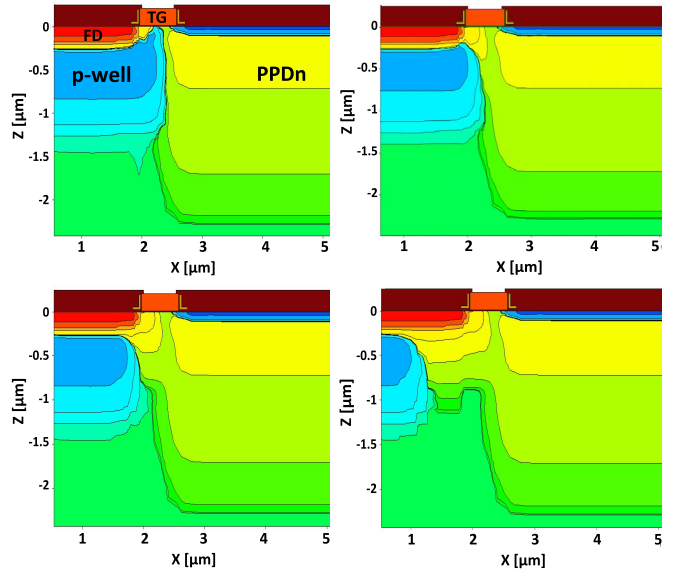

FIGURE 3. Doping concentration example, in the TG region, with different distances between p-well edge and TG edge. From left to right, from top to bottom the distance increases (dist1, dist2, dist3, dist4).

TABLE 1. Simulated impulse response time and static demodulation contrast of PPDs with different p-well-to-TG distances.

p-well to TG edge dist. [μm]	Imp. resp. time [ns]	Static demod. contrast
dist1	>300	100%
dist2	14	100%
dist3	4	100%
dist4	4	50%

barrier [14] and preventing the correct biasing and full-depletion of the PPD itself. In the second case (dist2), where the distance between p-well and TG is increased, the PPD is correctly biased but there is still a small potential barrier. In general, a potential barrier is particularly unwanted since it slows down the transfer of the charge to the FD and part of this charge remains in the PPD without being transferred, which would decrease the demodulation contrast. On the opposite side, a large distance between p-well and TG, e.g., dist4, would avoid the generation of any potential barrier by having a wider channel between PPD and FD. Although this helps to increase the charge transfer speed, it decreases the effect of modulation in the TG channel, since during the TG OFF phase the channel is still conducting, originating a reduction of the demodulation contrast. This can be seen in Fig. 5, where we plot the conduction band energy (CBE) with TG OFF, showing that the channel is indeed not properly closed.

Fig. 6 shows the simulated impulse response curve for the four distance cases whereas Table 1. summarizes the simulated impulse response times and static contrasts. It is clear that a good trade-off needs to be found depending on the specific technology.
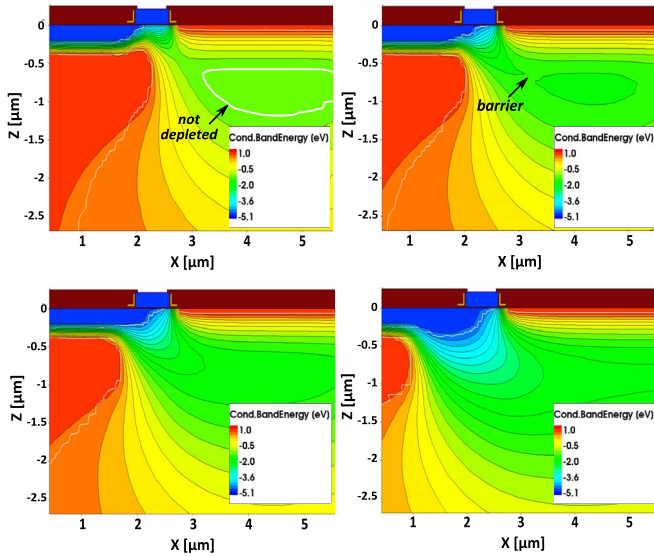
FIGURE 4. 3D TCAD simulations: cut-planes along vertical axis representing the conduction band energy in the TG region with TG ON. From left to right, from top to bottom the distance between p-well and TG edge increases (dist1, dist2, dist3, dist4).
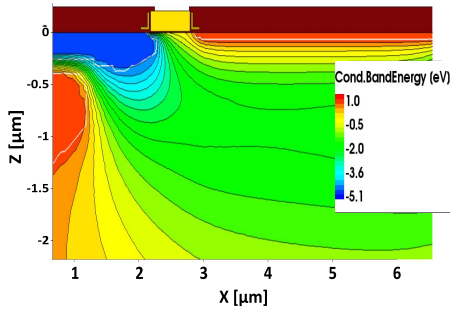

FIGURE 5. TCAD simulation of the conduction band energy, in the TG region, with TG OFF, with the largest distance from p-well to TG edge (dist4).
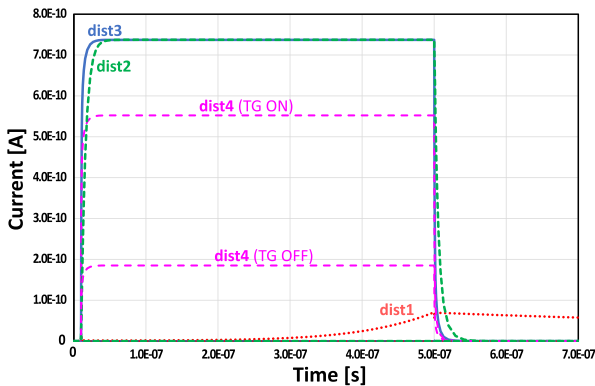

FIGURE 6. Simulated impulse response of PPD with different p-well to TG distance (dist1 to dist4).

B. THRESHOLD ADJUSTMENT IMPLANTS

Another optimization point for the TG region is the threshold adjustment implant. This can be particularly useful with high TG lengths. The threshold adjustment implant with proper
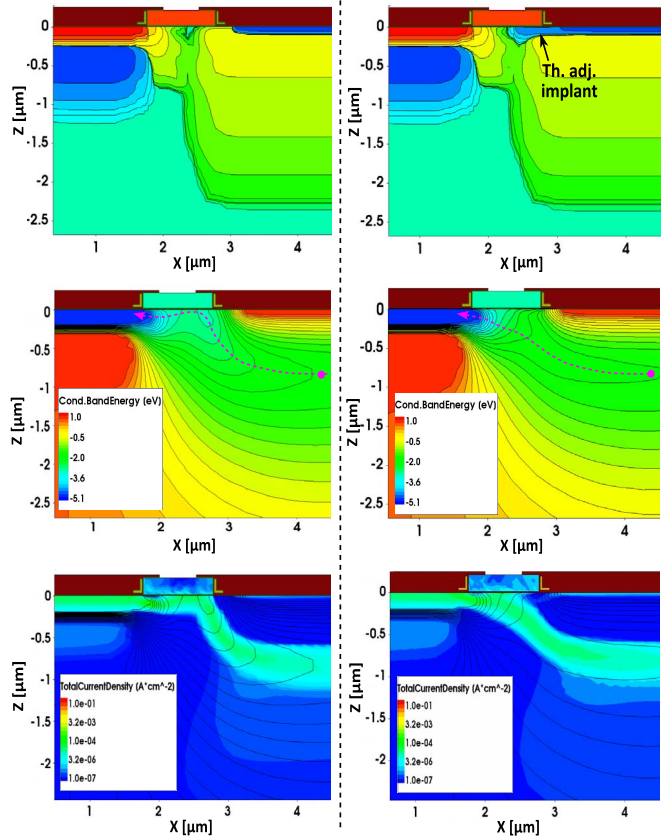

FIGURE 7. TCAD simulations without (left column) and with (right column) threshold adjustment implant. From top to bottom: doping concentration, CBE and current density.
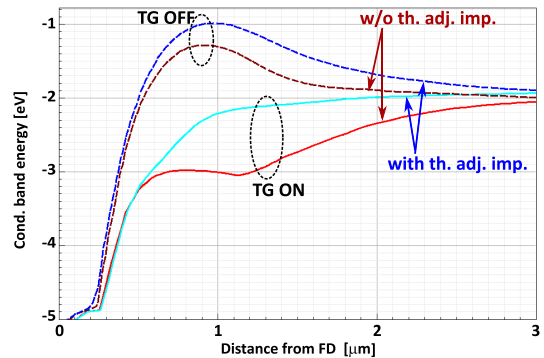

FIGURE 8. TCAD simulation of CBE along the carrier path, from FD (distance=0) to PPD center without and with threshold adjustment implant and with TG ON and TG OFF.

doping profile creates: i) a higher potential barrier when TG is OFF and ii) a linear potential gradient from the PPD to the FD when TG is ON, avoiding potential pockets [13], [14]. The latter is done by locally increasing the threshold only in one part of the TG [13].

TCAD simulation results (doping concentration and CBE) are reported in Fig. 7 for the PPD with and without the threshold adjustment implant. It can be seen that there is a small potential pocket in the first case and a linear carrier
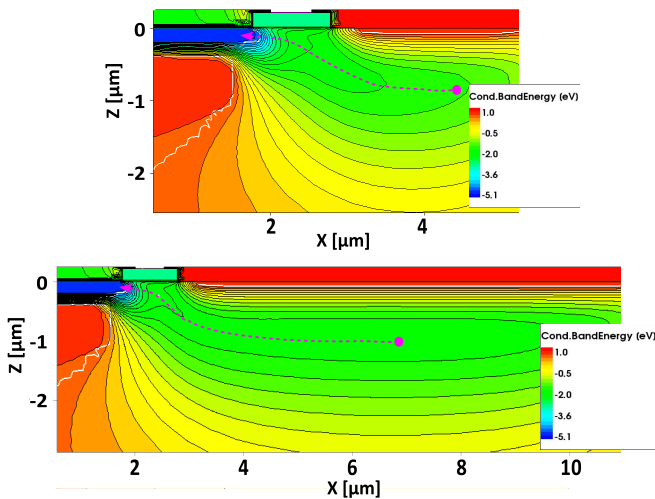
FIGURE 9. TCAD simulation of the conduction band energy in PPDs with two different lengths: short PPD length (top) and longer −3 times- PPD length (bottom). Carrier paths indicated with dashed lines.
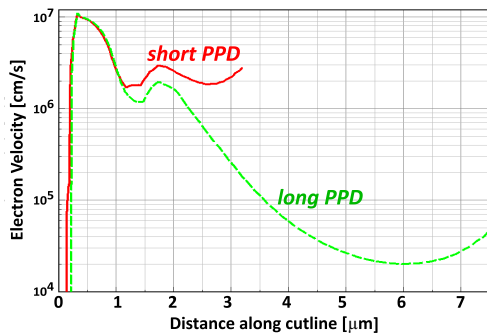

FIGURE 10. Simulation of electron velocity along the carrier path, from FD (distance= 0) to PPD center, of short and long PPDs.

path in the second case. Fig. 8 shows the CBE along the carrier path, from FD (distance=0) to PPD center (largest distance) in the two cases (with and without threshold adjustment implant) and with TG ON or OFF. This plot confirms that with this implant, the barrier is higher when TG is OFF and potential pockets are avoided.

C. PPD LENGTH

PPD length (represented in Fig. 2) is an important parameter, affecting the device performance. In general, a large PPD sensitive area is preferable to have a higher fill-factor (FF), resulting in a higher effective quantum efficiency. However, without particular shaping of the PPD this would result in a very low drift electric field at the center of the PPD, leading to a longer lateral transfer time. Moreover, depending on the PPDn implant, higher PPD lengths can result in a higher pinning voltage and a larger depleted region depth, which would reduce the vertical transfer time. Therefore, depending on the application and overall system, a good trade-off between QE and transfer time should be made and the PPD length should be chosen accordingly.
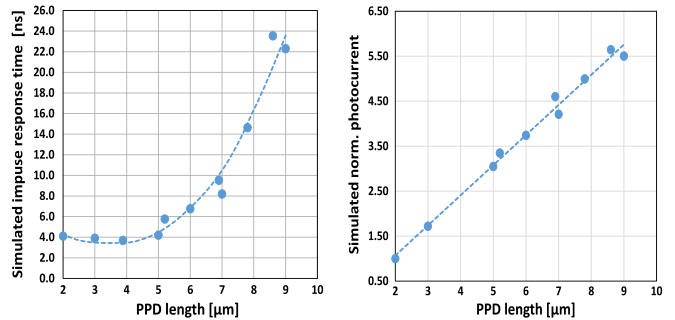

FIGURE 11. Simulated impulse response time (left) and photocurrent (normalized to the 2 μm case) (right) as a function of the PPD length.

In Fig. 9 we compare TCAD simulations of the CBE in two PPDs with different length (the longer one is 3 times larger than the other). It can be seen that in the shorter case, the CBE changes gradually in the entire PPD region, creating a significant drift electric field, and thus a higher electron velocity. Conversely, for the longer PPD in the central region (i.e., CBE well) the CBE is almost constant, thus creating a lower drift electric field as well as a low electron velocity. Fig. 10 shows the extracted electron velocities in the short and the long PPDs, along the carrier path (distance=0 at the FD). The electron velocity is more than one order of magnitude lower in the case of longer PPDs.

We have also simulated the transient behavior of PPDs with several lengths. In Fig. 11 we plot the impulse response time (left) and the normalized photocurrent (right). The normalized photocurrent increases almost linearly with the PPD length, so longer PPD lengths result in larger photocurrents. The impulse response time instead has a more interesting behavior: starting from the longest PPD and going toward smaller ones, it decreases when reducing the length of the device till reaching a minimum for the mid-lengths. In case of further reduction of the PPD length, the impulse response starts to slightly increase. A similar behavior has been previously reported in [15]. It could be related to the smaller pinning voltage resulted by a smaller PPD length, which reduces the depletion region depth and increases the vertical collection time. For very small PPD dimensions, the vertical collection time may become the dominant factor, notwithstanding the reduced horizontal transfer time.

D. PPD SHAPING

PPD shaping is one of the possible methods to cope with the increase in transfer time when using larger or longer PPDs. The shaping typically reduces the pinning voltage on one side of the PPD and not on the other side (generally close to the TGs). This creates a fast charge drift towards the PPD going to the TG region. When evaluating the shape of the PPD it is important to: i) create a drift electric field that is high enough, ii) to avoid possible potential barriers and iii) to push the PPD higher-potential region (i.e., the CBE well inside the PPD) as close as possible to the TG
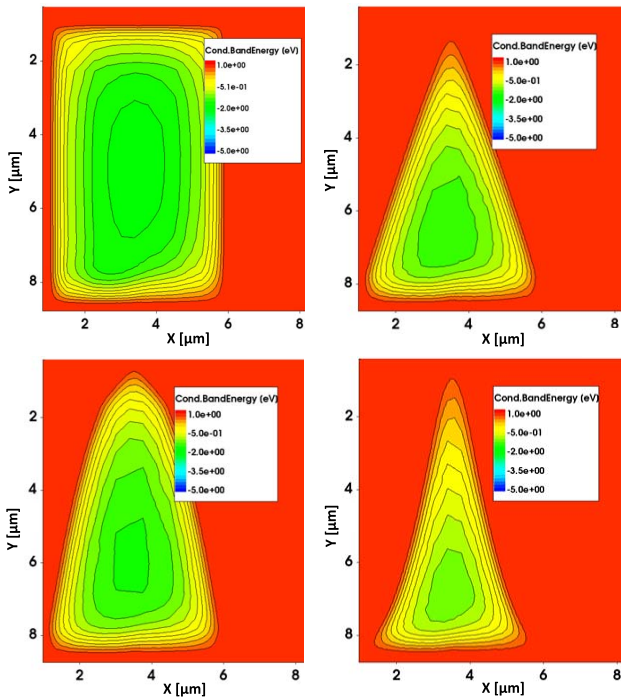
FIGURE 12. 3D TCAD simulation: horizontal cut-plane (parallel to the surface) of the conduction band energy (CBE) inside the shaped PPDs. Left to right, top to bottom: rectangular, triangular, convex and "bell" shape. It can be noted the different position of the minimum of CBE in the PPD region. In all structures the TGs and the FDs are at the bottom.
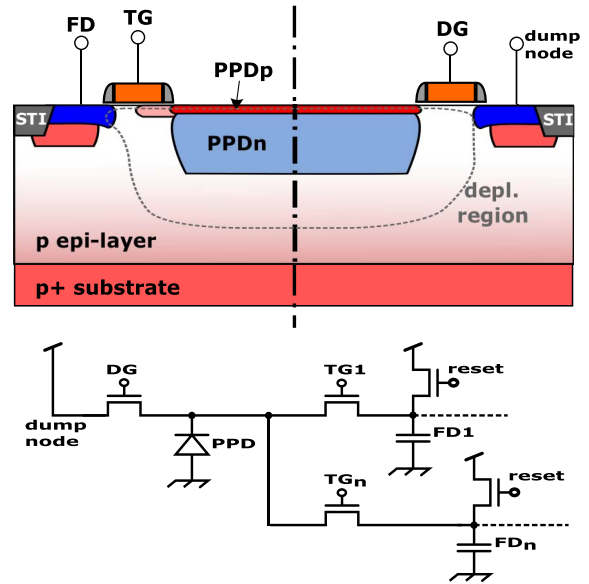

FIGURE 13. At the top, simplified cross-section of a PPD with transfer gate, FD, dump gate and dump node. The dump gate and dump node position can be different than in the figure. At the bottom, schematic representation of the device.

region, to speed up the charge transfer from the PPD to the FDs.

Within the scope of this work, we investigated four different shapes (see Fig. 12): rectangular (as reference), triangular, convex and "bell"-shaped PPDs for analyzing the impact of the PPD shape on charge transfer speed. In all these structures the TGs and the FDs are at the bottom (at high y coordinates). The PPD height-to-base ratio in all these structures is kept the same and approximately equal to 1.5. In these structures, the PPD length is higher than the width and the TG positioning is not optimal for the PPD performance, but this will highlight the differences with the PPD shape.

Fig. 12 shows the TCAD simulation of the conduction band energy inside the PPD. Among the shaped PPDs, convex shape has the advantage of maintaining a high FF while creating a drift field towards the TG. However, the maximum of potential in the PPD is still too far from the FD. This creates a potential barrier in the carrier path from the center of the PPD towards the FD. Conversely, "bell" and triangular shapes create a more linear pinning-voltage variation and thus a higher drift field. Moreover, the maximum of the potential, i.e., CBE well, is closer to the TG region. In the "bell"-shaped PPD it is the closest. This would result in a better potential gradient and a lower charge transfer time towards the FD.

We simulated the transient behavior of these structures with pulsed light illumination. The impulse response time of the rectangular PPD results very high, greater than 300 ns. This is due to the high PPD length combined with a small width, creating a small drift field and a small TG channel region. For the convex shape we obtained ~ 105 ns, whereas for the triangular and the bell shapes we obtained 9ns and 8 ns respectively.

E. DUMPING GATE
One of the challenges of all 3D systems today is the sunlight performance, in other words, the presence of strong background light. In particular during the readout phase, when the PPD is not biased and not depleted, the background light is still active and continuously generates charges in the PPD region. As a result, it is possible that the photo-generated charges in the PPD spill out into the collection region and alter the signal that is being read-out. To avoid or minimize such situation, the PPD-based ToF pixels can benefit from a charge draining node, using a drain diffusion [17], [18] and a dumping gate, which connects the PPD to the dump diffusion. The cross section of a pixel with a dump gate (DG) can be seen in Fig. 13.

The design of the DG region is different to the one of the TG region. The charge transfer through the DG does not need to be as fast as in the TG. Its function is to keep the PPD biased and to drain the photo-generated charges outside the PPD region. However, the DG and dump node would reduce the fill-factor of the pixel and if not properly designed, would impact the performance of the pixel during modulation. Thus, a careful analysis of the design of the dump gate and dump diffusion node are needed.
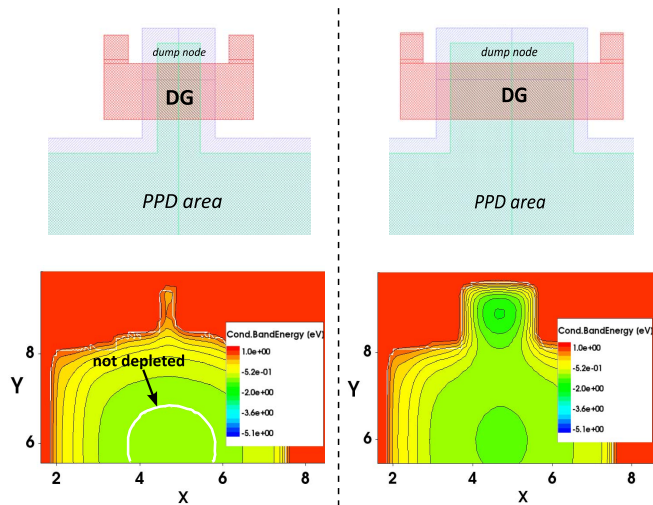
FIGURE 14. Representation and TCAD simulation of the CBE of two DG solutions. On the left, for small DG and dump node regions. On the right, for larger dump gate and node areas.

FIGURE 15. Simulations of photocurrent ($\lambda = 940$nm) (left) and transit time (right), both normalized to the 8 μm case, as a function of the epitaxial layer thickness.

the transfer speed. In a triangular PPD, the dump gate and the dump node can be placed on the side of the triangle. The drift electric field would not help transferring the charge in the PPD close to the DG, but as written previously, the transfer of the charge towards the dump node does not need to be as fast as towards the FD.

F. EPITAXIAL LAYER THICKNESS
Epitaxial layer thickness is another important trade-off parameter in PPD design. In a PPD structure like the one in Fig. 2, the epi-layer thickness can be the limiting factor of the depleted-region depth. This affects the achievable QE, especially at high wavelengths, and the vertical transit time of generated carriers. Indeed, the higher is the epi thickness, the higher will be the collection depth. This improves the QE, but carriers photogenerated at high depth in the epi layer have to diffuse and drift towards a longer path, possibly increasing the overall impulse response time of the PPD.

Fig. 15 shows the simulated values of the photocurrent in the PPD (excitation light with a wavelength of 940 nm) and the normalized transit time (normalized to the 8 μm case) as a function of the epitaxial layer thickness. Both parameters increase with the epi-layer thickness, however, while the photocurrent increases linearly, the transit time increases almost linearly for thin epi layers, but then it increases exponentially for thicker epi-layers. This could be related to a more and more important part of the epi-layer not depleted and without any gradient of the doping profile: in such region the carrier can only move by diffusion, being much slower than the one moving by drift. Depending on the application requirements and on the actual doping profiles in the PPD, the proper trade-off on epi-layer thickness should be identified between QE and transfer speed of the PPD.

IV. MEASUREMENT AND SIMULATIONS VALIDATION
Based on the optimization of the TG region and of the PPD shape described in the previous chapter, we produced chips containing different versions of PPD arrays. The pitch of the pixels is 10μm $\times$10μm, with a nominal fill-factor between ~15% and ~30%. In this section, we will report the experimental results of these pixels and compare them

From TCAD simulations, it is clear that the PPD area has to be relatively small (in particular the PPD length) to have a fast charge transfer. The space for the addition of a DG is reduced. However, as for the TG, also the DG channel width cannot be too small, in order to work properly. Thus, both the dimensions of the DG and dump diffusion need to be adjusted.

We simulated two cases: one with a small DG channel width and another with a larger DG channel width (3 times larger, which is close to the maximum allowed dimension considering the best PPD length obtained in the previous section). Fig. 14 shows the representation of the DG regions and the corresponding TCAD simulations of the CBE, in the horizontal cut-plane. In the first case, the DG is too small and the PD region is not depleted with DG ON, thus the charge dumping does not work properly. In the second case, the PPD region is fully depleted, but the CBE plot shows a small potential barrier, indicating that the DG should possibly be designed larger. However, this second solution would work even with the potential barrier and the PPD charge during read-out can be transferred to the dump node.

For the second DG solution we estimated the effective charge transfer speed. We simulated a PPD with two DGs on opposite sides. With a constant background light, we turned the DGs ON at t=0s and evaluated the charge inside the PPD at different times. Multiplying this charge by the simulated FD capacitance we obtained the estimated offset in the case of DGs ON for a specific amount of time. Results showed that it starts to deplete the PPD quickly but never reach a complete depletion. After about 50 μs the remaining charge produces an offset of about 5mV in the FD.

One possible solution to have a bigger DG without worsening the performance, could be enlarging the PPD but having it shaped. The higher PPD length would allow inserting a relatively large DG while the shaping avoids worsening
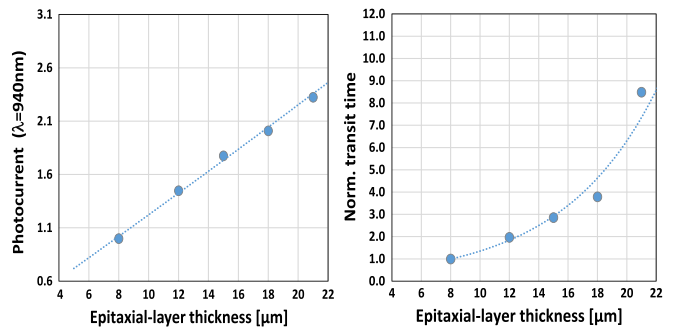
with the simulation results. We performed three types of measurements:

- *Quantum efficiency:* we used a setup based on a broadband lamp, a monochromator and a calibrated photodiode. With the PPD pixels working in standard conditions and with continuous wave (CW) illumination, we extracted the signals at the collection node as a function of the integration time, thus obtaining the photocurrent generated inside the PPD and then the QE knowing the number of photons impinging the PPDs.

- *Demodulation contrast:* when the PPD-based ToF detector is working in demodulation mode, with modulation of the light, four different samples of the reflected light-waveform have been acquired, and the demodulation calculated following Eq. (3), as reported in [1] and [4].

- *Impulse response time:* The PPDs were operating in dynamic mode (toggling the TG ON and OFF) with a frequency of 1MHz. We shined the detector with a sharp laser pulse (width <100ps FWHM, wavelength=830nm) and we moved the laser excitation in time with respect to the TG toggling time (see the sketch in Fig. 17). For each laser time-position, we collected the signal from the FDs after the accumulation of several pulses. We plotted them as a function of the laser-pulse time delay, obtaining two curves that cross around the TG crossing time (see Fig. 18). We quote the impulse response time of the PPD as the speed of this transition (10%-90%). When measuring the impulse response of the detector both the TG transfer time and the collection time for carriers from the epitaxial layer are included.

A. QUANTUM EFFICIENCY

We implemented the different PPD pixels on several epi/substrates in order to compare their performance. Fig. 16 shows the measured QE of PPD pixel arrays with 8 μm, 12 μm, 18 μm epi-layer thickness, compared to the final optimized structure. Moving from 8 μm to 18 μm, the QE at 850 nm increases significantly, from ∼20% to more than 30% (averaging the oscillations due to the dielectric stack on the top of the active area). With the final optimized one we obtained a QE of ∼45% at 850nm (∼40% averaging the oscillations), ∼30% at 900nm and ∼20% at 950nm.

B. DEMODULATION CONTRAST AND IMPULSE RESPONSE TIME

We measured the demodulation contrast for the triangular shaped and the "bell" shaped PPDs, obtaining ∼64% at a frequency of 40MHz. In this particular measurement, we wanted to identify just the pixel demodulation contrast, thus we used a fast Vertical-Cavity Surface Emitting Laser (VCSEL), modulated with an external fast-pulser (Agilent 81150A), using strong square-wave modulation pulses, synchronized with the acquisition system. With these devices we measured also the impulse response time.
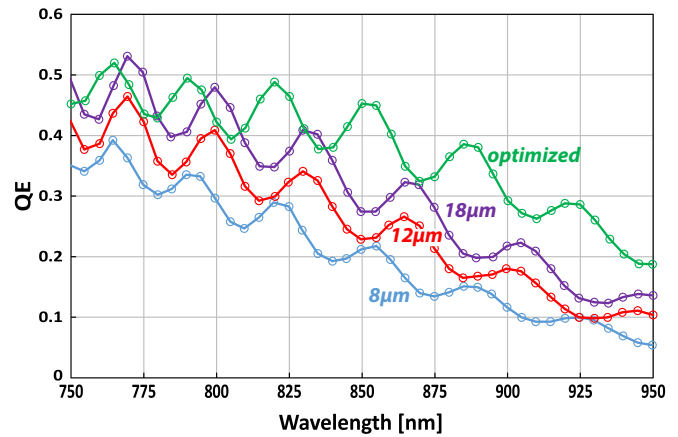

FIGURE 16. Measured QE of the PPD arrays, with 10 μm x 10 μm pitch, on structures with different epi-layer thickness: 8 μm, 12 μm, 18 μm and the final optimized one.
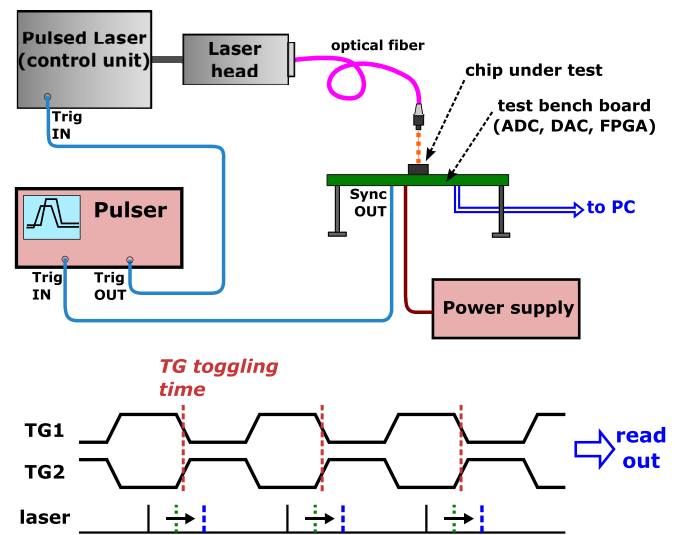

FIGURE 17. Setup for impulse response time measurement. Sync signal from the test-bench-board (synchronous with TGs) is used to trigger the pulser, which, with an adjustable delay, triggers the laser pulse. The delay is changed, crossing the time when TG1 and TG2 toggle. Eventually, the FD signals as a function of time delay are plotted.

For the rectangular shape PPD we obtained a very high impulse response time, higher than the specific measurement full scale. Conversely, for the "bell"-shaped PPD we obtained about 8 ns 10%-90%, in agreement with the TCAD simulations.

We measured and compared also the performance of rectangular PPDs with smaller areas and with variable length, as the ones in Fig. 9 and Fig. 11. In particular we measured the impulse response time and the demodulation contrast. The latter one has been measured in this case with the real system environment, i.e., including the actual modulated illuminator.

Fig. 19 shows the measured FD signals as a function of the time. It can be clearly seen that the charge transfer in the PPD gets slower and slower as the PPD length increases. The fastest one has an impulse response time of about 4 ns,
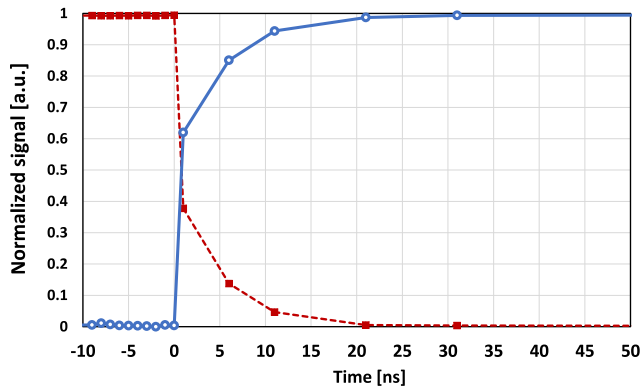
FIGURE 18. Measured impulse response of PPD bell-shaped, obtained with a laser excitation (<100ps FWHM, λ = 830nm) and moving the laser excitation in time with respect to the TG toggling time. Normalized FDs signals are plotted. The rise time (10%-90%) of blue-continuous curve is ~8ns.
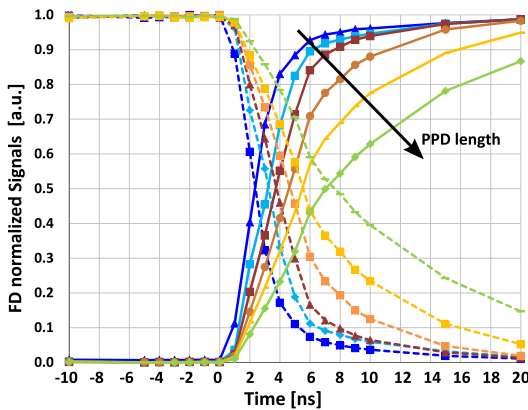

FIGURE 19. Measured impulse response time of rectangular PPDs with different lengths. From the faster to the slower: 3.9 μm, 5.2 μm, 6.0 μm, 6.9 μm, 7.8 μm, 8.6 μm. The speed is monotonically decreasing with PPD length increment.

which is a very good value, whereas the slowest one has 20 ns.

Table 2 compares the simulated and the measured impulse response time (10%-90%) of the PPDs with different lengths, together with the measured demodulation contrast at 40 and 80 MHz. It can be seen that there is a good agreement between the simulation and the measurement results, with a slight overestimation of the worsening with high lengths by the simulation with respect to the measurements. Concerning the demodulation contrast, we obtained 68% at 40 MHz and 47% at 80 MHz for the fastest PPD. The demodulation contrast becomes worse increasing the PPD length due to the increment of the impulse response time, resulting in a value of 0% at 80 MHz for the largest length (in that case, the impulse response time is higher than 20ns). The combination of a high modulation frequency with a slow transfer of charge causes that part of it remains in the PPD when the TGs are toggled, eventually being collected by the wrong FD and thus, reducing the demodulation contrast.

TABLE 2. Simulated and measured impulse response time and measured demodulation contrast obtained with rectangular PPDs, with different lengths.

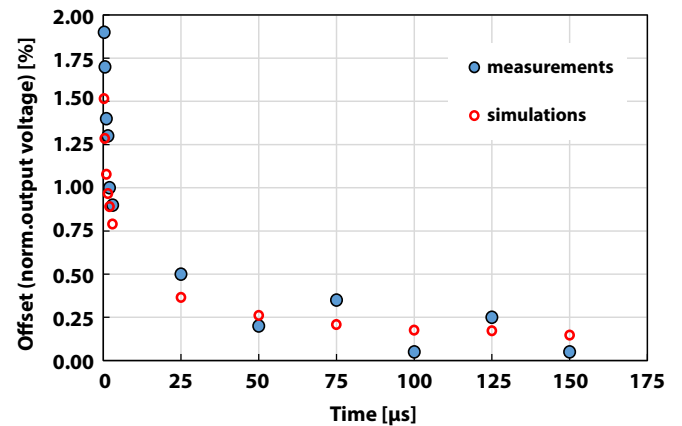| PPD length [μm]	Simulated imp. Resp. time [ns]	Measured imp. resp. time [ns]	Demod. Cont. @40MHz	Demod. Cont. @80MHz
3.9	3.7	4	68%	47%
5.2	5.77	5	61%	40%
6.0	6.77	6	58%	36%
6.9	9.52	11	52%	27%
7.8	14.6	16	44%	18%
8.6	23.6	20	32%	0%

FIGURE 20. Variation of the offset inside the collection-node, when opening the TG (expressed as percentage of the maximum output voltage) as a function of the time when the DG is ON (before opening the TG). Comparison of the results obtained experimentally and by TCAD simulation.

C. DUMP GATE SPEED

We measured the depletion speed of the dump gate. We considered the bigger one, as shown on the right side of Fig. 14. In this case the measurement procedure is as follows: the PPD is filled to the point of overflow the FDs, then the RST pulse is applied to reset the FD node. After that, the DG is pulsed (with different pulse durations) to dump the charge in the PPD to the dump node. Finally, the TG is toggled ON again to "read" out the charge left in the PPD. The signal in the FD is then plotted as a function of the DG pulse duration.

Fig. 20 compares the results of the measurements with the simulations described in the previous chapter. There is a good agreement and both highlight that after 50 μs the remaining offset measured in the FD is smaller than 0.25% of the maximum output voltage.

V. CONCLUSION

We described several optimizations for pinned photodiodes designed for iToF sensors, where the transfer speed and the QE in the NIR are important parameters. In the TG region we optimized the p-well mask position and we discussed possible threshold adjustment implants to speed up the charge

transfer. The PPD dimensions are also important: a large PPD is preferable to have high FF and high QE, but it is also important to have a fast collection of charges. Thus, a trade-off for the PPD length has to be found. In our study, we obtained that a PPD length between 4μm and 5μm is the best trade-off. An alternative option to have fast but bigger PPDs is to change the PPD shape. PPD shaping creates a drift field within the device and pushes the maximum potential region in the PPD towards the FD. In our study the bell-shaped PPD had the best transfer speed, thus the fastest impulse response time.

We produced and measured chips containing different arrays of PPDs, with a pitch of 10μm ×10μm, with FF between 15% and 30%. We measured the QE, the demodulation contrast and the impulse response time. This last type of measurement is interesting to have a direct estimation of the PPD speed and to have a direct comparison with the TCAD simulation results.

All the optimizations described in this paper have been combined together leading to a final pixel with better performances. This pixel includes the optimal distance of p-well as in Fig. 4, the threshold adjustment implant in the TG region as in Fig. 7, and with a sensitive area of 16 μm^2. We obtained a QE of ~45% at 850nm and ~30% at 900nm, with a FF of 30%. The demodulation contrast measured with the real-system illuminator is ~70% at 40 MHz and about 50% at 80MHz. We used a square wave modulation, which increasingly approximated to a sinusoidal function when operating at higher frequencies. The good performance are due to the fast transfer speed: the impulse response time of this pixel, which is about 4ns.

REFERENCES

[1] F. Remondino and D. Stoppa, *TOF Range-Imaging Cameras*. Heidelberg, Germany: Springer-Verlag, 2013.
[2] B. Buttgen and P. Seitz, "Robust optical time-of-flight range imaging based on smart pixel structures," *IEEE Trans. Circuits Syst. I, Reg. Papers*, vol. 55, no. 6, pp. 1512–1525, Jul. 2008.
[3] R. Lange and P. Seitz, "Solid-state time-of-flight range camera," *IEEE J. Quantum Electron.*, vol. 37, no. 3, pp. 390–397, Mar. 2001.
[4] R. Lange, P. Seitz, A. Biber, and S. C. Lauxtermann, "Demodulation pixels in CCD and CMOS technologies for time-of-flight ranging," in *Proc. Sensors Cameras Syst. Sci. Ind. Appl. II (SPIE)*, vol. 3965. San Jose, CA, USA, 2000, pp. 177–188.
[5] B. Büttgen, T. Oggier, M. Lehmann, R. Kaufmann, and F. Lustenberger, "CCD/CMOS lock-in pixel for range imaging: Challenges, limitations and state-of-the-art," in *Proc. 1st Range Imag. Res. Day*, Zürich, Switzerland, 2005, pp. 21–32.
[6] D. Van Nieuwenhove, W. Van Der Tempel, and M. Kuijk, "Novel standard CMOS detector using majority current for guiding photo-generated electrons towards detecting junctions," in *Proc. IEEE/LEOS Symp. Benelux Chapter*, Brussels, Belgium, 2005, pp. 229–232.
[7] L. Pancheri *et al.*, "Current assisted photonic mixing devices fabricated on high resistivity silicon," in *Proc. IEEE Sensors*, Lecce, Italy, 2008, pp. 981–983.
[8] C. Tubert *et al.*, "High speed dual port pinned-photodiode for time-of-flight imaging," in *Proc. IISW*, Bergen, Norway, 2009, pp. 357–360.
[9] L.-E. Bonjour, T. Baechler, and M. Kayal, "High-speed general purpose demodulation pixels based on buried photodiodes," in *Proc. IISW*, Hokkaido, Japan, 2011, pp. 1–4.
[10] D. Stoppa *et al.*, "An 80 x 60 range image sensor based on 10um 50 Mhz lock-in pixels in 0.18um CMOS," in *Proc. ISSCC*, San Francisco, CA, USA, Feb. 2010, pp. 406–407.
[11] S.-J. Kim *et al.*, "A three-dimensional time-of-flight CMOS image sensor with pinned-photodiode pixel structure," *IEEE Electron Device Lett.*, vol. 31, no. 11, pp. 1272–1274, Nov. 2010.
[12] B. Rodrigues *et al.*, "Indirect ToF pixel integrating fast buried-channel transfer gates and gradual epitaxy, and enabling CDS," in *Proc. IISW*, Hiroshima, Japan, 2017, pp. 266–269.
[13] L. Yiqiang *et al.*, "Charge transfer efficiency improvement of a 4-T pixel by the optimization of electrical potential distribution under the transfer gate," *J. Semicond.*, vol. 33, no. 12, Dec. 2012, Art. no. 124004.
[14] E. R. Fossum and D. B. Hondongwa, "A review of the pinned photo-diode for CCD and CMOS image sensors," *IEEE J. Electron Devices Soc.*, vol. 2, no. 3, pp. 33–43, May 2014.
[15] Y. Xu and A. J. P. Theuwissen, "Image lag analysis and photodiode shape optimization of 4T CMOS pixels," in *Proc. IISW*, Snowbird, UT, USA, 2013, pp. 153–157.
[16] B. Shin, S. Park, and H. Shin, "The effect of photodiode shape on charge transfer in CMOS image sensors," *Solid-State Electron.*, vol. 54, no. 11, pp. 1416–1420, Nov. 2010.
[17] H.-J. Yoon, S. Itoh, and S. Kawahito, "A CMOS image sensor with in-pixel two-stage charge transfer for fluorescence lifetime imaging," *IEEE Trans. Electron Devices*, vol. 56, no. 2, pp. 214–221, Feb. 2009.
[18] D. Durini *et al.*, "Experimental comparison of four different CMOS pixel architectures used in indirect time-of-flight distance measurement sensors," in *Proc. IISW*, Jun. 2011, pp. 165–168.

FABIO ACERBI (S'12–M'13) was born in Carpi, Italy, in 1984. He received the bachelor's degree in electronics engineering from the University of Modena e Reggio Emilia, Modena, Italy, in 2006, the master's degree in electronics engineering and Ph.D. degree in information technology from Politecnico di Milano, Milan, Italy, in 2008 and 2012, respectively. From 2009 to 2013, he was with Politecnico di Milano engaged in the development and characterization of new InGaAs/InP single-photon avalanche diodes. Since 2013, he has been with FBK, Trento, Italy, on the development of new silicon photomultipliers and SPAD technologies and the related readout electronics. He also works on the design, TCAD simulation, and characterization of photodetectors for ToF applications.

MANUEL MORENO-GARCIA (M'16) was born in Sevilla, Spain, in 1986. He received the B.Sc. degree (with the National Award for Excellence in Academic Performance) from the University of Sevilla, Spain, in 2009, the M.Sc. degree in nuclear physics and microelectronics from the WWU Münster, Germany, and Universidad de Sevilla, Spain, in 2009 and 2011, respectively, and the Ph.D. degree from the Instituto de Microelectronica de Sevilla, Sevilla, in 2015. Since 2015, he has been with the Integrated Radiation and Image Sensors Research Unit, FBK. His research interests are PPD and SPAD-based sensors, and the simulation, design, and characterization of semiconductor photon detectors for ToF imaging.

GÖZEN KÖKLÜ received the B.Sc. degree in microelectronics engineering from Sabanci University in 2007, the M.Sc. degree from the Electrical Engineering Department, Ecole Polytechnique Federale de Lausanne (EPFL), in 2009, and the Ph.D. degree from EPFL in 2014 after completing her research work on the topic of design and implementation of CMOS image sensors for biomedical applications with the Integrated Systems and the Microelectronic Systems Laboratories, EPFL (LSI and LSM). Since 2014, she has been pursuing her career in Heptagon Advanced Micro-optics (part of AMS AG), working toward the design and implementation of new generation Time of Flight cameras and leading the IC design team.

RADOSLAW MARCIN GANCARZ was born in Debica, Poland, in 1973. He received the M.Sc.Eng. degree in electronics from the Wroclaw University of Science and Technology in 1999. Since 2000, he has been an Analog/Mixed-Signal Design Engineer for various semiconductor design companies. In 2009, he joined ESPROS Photonics, where he worked on backside illuminated iTOF IC systems. In 2015, moved to HEPTAGON, where he continued to work on development of iTOF ICs.

BERNHARD BÜTTGEN (M'11) received the Diploma degree in electrical engineering from the University of Siegen in 2002 and the Ph.D. degree in microtechnology from the University of Neuchatel, Switzerland, in 2006.

He has been with Heptagon since 2014, where he worked on 3-D system architecture design and on the company's 3-D imaging strategy. In 2014, he became an employee of AMS as a result of the acquisition of Heptagon. He developed long-term experience on time-of-flight imaging during his time with CSEM and MESA Imaging and his post-doctoral activity at TU Delft. He is currently with Apple, Cupertino, CA, USA.

ALICE BIBER was born in Boston, MA, USA, in 1967. She received the B.S. and M.S. degrees from the Massachusetts Institute of Technology in 1989 and 1990, respectively, and the Ph.D. degree from the Swiss Federal Institute of Technology, Switzerland, in 2000. Her Ph.D. thesis was titled "Avalanche photodiode image sensing in standard silicon BiCMOS technology." She was a mixed signal IC designer for several companies before she joined Heptagon in 2016 to work in the field of image sensing.

DANIEL FURRER was born in Baden, Switzerland, in 1980. He received the M.Sc. degree in electrical engineering and information technology from ETH Zurich in 2005. He was an analog/mixed signal Design Engineer for various semiconductor design companies before he joined Mesa Imaging in 2014, where he worked on image sensors for ToF applications.

DAVID STOPPA (SM'12–M'97) received the Laurea degree in electronics engineering from the Politecnico di Milano, Italy, in 1998 and the Ph.D. degree in microelectronics from the University of Trento, Italy, in 2002. In 2017, he joined AMS, where he is in charge of the research and development of next generation range-sensors. From 2014 to 2017, he was the Head of the Integrated Radiation and Image Sensors Research Unit at FBK, where he has been working as a Research Scientist since 2002 and as a Group Leader of the Smart Optical Sensors and Interfaces group from 2010 to 2013. From 2002 to 2012, he has been teaching courses on analogue electronics and microelectronics with the Telecommunications Engineering Faculty, University of Trento. His research interests are mainly in the field of CMOS integrated circuits design, image sensors, and biosensors. He has authored or co-authored over 120 papers in international journals and presentations at international conferences, and holds several patents in the field of image sensors. He was a recipient of the 2006 European Solid-State Circuits Conference Best Paper Award. Since 2011, he has been serving as a Program Committee Member of the International Solid-State Circuits Conference (ISSCC) and the SPIE Videometrics, Range Imaging, and Applications Conference, and was a Technical Committee Member of the International Image Sensors Workshop in 2009, 2013, 2015, and 2017. He was a Guest Editor for the IEEE JOURNAL OF SOLID-STATE CIRCUITS special issues on ISSCC'14 in 2015 and he has been serving as an Associate Editor since 2017.